Enhanced charge carrier separation to improve hydrogen production efficiency by ferroelectric spontaneous polarization electric field

Xueyan Huang[a], Kaiqiang Wang[a], Yaozhu Wang[a], Bo Wang[a], Lulu Zhang[a], Fan Gao[a], Yan Zhao[a], Wenhui Feng[b], Shiying Zhang[b], Ping Liu[a,*]

[a] Research Institute of Photocatalysis, State Key Laboratory of Photocatalysis on Energy and Environment, Fuzhou University, Fuzhou 350002, PR China
[b] Hunan Provincial Collaborative Innovation Center for Environment and Energy Photocatalysis, Changsha University, Changsha 410022, PR China

ARTICLE INFO

ABSTRACT

Ferroelectrics with internal polar domains has been utilized to enhance photoinduced carriers separation for improving photocatalytic performance by combining them with metal-sulfide semiconductor material. Herein, we construct a new nanohybrid photocatalyst, which combines ferroelectric n anospheres (BaTiO$_3$) and semiconductor nanoparticles (CdS). This hybrid photocatalyst exhibits remarkable hydrogen production activity. The optimum hydrogen production rate based on BaTiO$_3$-CdS composite structure reaches 483 μmol h^{-1} g^{-1}, which is about 9.7 times greater than that of pristine CdS. The observations indicate that charge carriers generated in CdS, more efficiently migrate to the surface and participate in the redox reactions, influenced by dipolar fields in the ferroelectric domains of BaTiO$_3$. These mechanistic insights will widen our fundamental understanding of charge separation and transfer processes to steer charge flow in a desired and efficient manner.

1. Introduction

The search for new alternative energy sources is a matter of global urgency due to the worldwide desire to decrease the use of fossil fuels and reduce accompanying environmental problems. Direct conversion of natural solar energy to H$_2$ fuel from water via photocatalysis is considered to be a potential technology to sustain the future development of our planet [1,2]. Despite myriad semiconductor systems, including TiO$_2$ [3–6], ZnO [7–10], and WO$_3$ [11–14], have been exploring, the current efficiency of photocatalysis is still far from being satisfactory. It is known that efficient absorption of available sunlight, fast electron-hole migration and separation, and abundant surface adsorption and active sites are crucial factors for achieving high-performance photocatalytic hydrogen reduction. In general, charge carrier separation remains the most complex and critical issue [15,16]. So far much work has focused on constructing new multiternary semiconductor materials for improving carrier separation efficiency. For instance, the use of co-catalysts can promote the separation of photogenerated charge carriers, and lower the barrier for hydrogen evolution reaction effectively [17–21]. However, It is well known that recombination of electron-hole pairs in the bulk materials merely requires several picoseconds, which is much faster than charge transportation and charge-consuming catalysis [22]. That is to say, most of the photogenerated electrons and holes prefer recombining with each other in

the bulk before reaching the surface of photocatalyst. As a result, only few electrons and holes are available for the surface catalytic reactions after transferring to a co-catalyst. Thus, co-catalyst strategy cannot improve charge separation in the bulk of semiconductor significantly, although which is capable of intensifying charge separation on the surface of photocatalyst effectively. In this context, the driving force to directly separate and transport bulk charges is the most critical factor [23,24]. Therefore, it is imperative to develop strategies to boost charge carriers separation for the applications of semiconductor photocatalysis.

Recent studies indicate that the internal electric field in photocatalyst particles can improve the efficiency of photocatalytic process. The presence of the internal electric field provides a driving force for the transport of photoinduced charge carriers, thus facilitating their separation [25–29]. Zhang et al. incorporated carbon into the Bi$_3$O$_4$Cl lattice to increase internal electric field for boosting bulk charge separation [23]. Recently, the ultrasonication-assisted piezoelectric polarization of ZnO nanorods was demonstrated to be capable of enriching the photo-generated carriers on the local surface of photocatalyst, hence the local density of photo-generated electrons and the selectivity of methane production were increased [30]. Among various photocatalytic materials containing internal electric field, ferroelectric materials possess strong inversion symmetry breaking with a spontaneous electric polarization, which could serve to promote the separation of

photoexcited carriers. The spatial selectivity of photochemical reactions of ferroelectric materials has been studied on BaTiO$_3$ [26,31–33], BiFeO$_3$ [34], and Pb(Zr$_{0.3}$Ti$_{0.7}$)O$_3$ (PZT) [35,36]. The mechanism of the spatially selective reactivity is thought to be the spontaneous in the ferroelectric domains, which bends the bands of electronic states so that photogenerated electrons and holes are transported in opposite direction. Hence, internal polar domains from ferroelectric materials can serve as permanent and controllable internal electric fields. Furthermore, ferroelectrics with an intrinsic build-in electric field have been utilized to enhance photoelectron properties simply by combing them with traditional semiconductor materials. A variety of studies have demonstrated that the appearance of ferroelectric materials can modulate the performance of semiconductor devices [37–39]. For instance, Wang et al. reported a largely enhanced performance of photoelectrochemical (PEC) photoanodes by ferroelectric polarization-endowed band engineering on the basis of TiO$_2$/BaTiO$_3$ core/shell nanowires (NWs) [40]. Similarly, Wang et al. have constructed Ag$_2$O–BaTiO$_3$ hybrid photocatalyst to enhance photoactivity though ferroelectric spontaneous polarization electric field by ultrasonic-wave-generated piezo-phototronic effect [29]. In addition, Cui et al. demonstrated BaTiO$_3$/α-Fe$_2$O$_3$ photocatalytic performance enhancement was associated with improved charge-carrier separation at the interface between the ferro-electric surface and the hematite [41]. However, mentioned above photocatalytic reaction were all induced by UV light irradiation (the band gap for BaTiO$_3$ is 3.2 eV) [42], so conventional heterojunction, charge transfer between two semiconductors due to matched energy band structures, may be responsible for the performance enhancement. Although there is no doubt that the effective influence of the internal electric field on the enhanced photocatalytic performance, the mechanism of the internal electric field on the semiconductor charge carrier separation is still undisclosed. In order to demonstrate the separation and migration of photogenerated charge carriers is greatly affected by internal electric field, heterojunction effects must be excluded. One possible solution is to ensure that one of the two semiconductors is not excited by light.

Herein, we propose to constructed ferroelectric BaTiO$_3$ nanospheres and photocatalyst CdS to form an BaTiO$_3$-CdS hybrid photocatalyst. CdS is one of the most popular visible light response photocatalysts because of its suitable band gap (~2.4 eV) [43]. The conduction-band edge potential of CdS is more negative than the reduction potential of H$_2$O/H$_2$, therefore, it preferably reduces protons (H$^+$) to H$_2$ gas. Unfortunately, ultrafast photoexciton recombination restricts pristine CdS photocatalyst from being extensively utilized [44–47]. The spontaneous polarization potential of BaTiO$_3$ nanocrystals can be applied to provide a build-in electric field. Therefore, the build-in electric field, as the driving force, can directly accelerate the separation of the photogenerated charge carriers in CdS particles. The hydrogen production rate of BaTiO$_3$-CdS is up to 482.92 μmol h^{-1} g^{-1} under visible light irradiation, which is about 9.7 times greater than that of pure CdS.

2. Experimental

2.1. Preparation

2.1.1. Materials

All the chemical precursors and solvents, including tetra-butyl titanate, ammonium hydroxide, barium hydroxide octahydrate (Ba(OH)$_2$·8H$_2$O, 98%), ethyl alcohol 98%, Zinc acetate dihydrate (Zn(CH$_3$COO)$_2$·2H$_2$O) and, thiourea (CH$_4$N$_2$S), were purchased from chemical suppliers and were used without further purification. Deionized (DI) water used in the synthesis came from local sources.

2.1.2. BaTiO$_3$ synthesis

We adopted a sol-gel hydrothermal method for the preparation of the BaTiO$_3$ nanoparticles. The preparation process is as follows [48]: First, 5 mL of ethyl alcohol and 5 mL de-ionized water were added into a 50 mL round bottom flask containing 0.025 mol of tetra-butyl titanate under magnetic stirring at 80 °C. Then, 4 mL ammonium hydroxide was added to the above solution. Simultaneously, 3.75 M barium hydroxide octahydrate (Ba(OH)$_2$·8H$_2$O, 98%) aqueous solution (10 mL) was kept at 80 °C using water bath to form homogenous solution. Subsequently, barium hydroxide octahydrate solution was added to the above round bottom flask, and continued vigorously stirring it for 20 min at 80 °C. The final suspension was transferred to a 100 mL Teflon-lined stainless-steel autoclave with a fill factor of 60%. The autoclave was heated to 200 °C for 24 h and then cooled to room temperature. The resultant products were filtered and washed several times with distilled water and ethanol, and then dried in air at 60 °C for 24 h.

2.1.3. BaTiO$_3$/CdS composite synthesis

Preparation of BaTiO$_3$-CdS (BaTiO$_3$:CdS = 10:2) composite by chemical bath deposition method. 400 mg of BaTiO$_3$ sample was added in 40 mL solution containing 148 mg cadmium acetate dihydrate (Cd(CH$_3$CO$_2$)$_2$·2H$_2$O). The obtained suspension was stirred for 30 min in dark to achieve the preferential absorption of Cd ion on the surface of BaTiO$_3$. 80 mg thiourea (CH$_4$N$_2$S) was then added to the suspension. After the chemical bath deposition at 80 °C for 30 min, the BaTiO$_3$-CdS product was collected by centrifugation and washed with de-ionized water several times to remove dissolvable ionic impurities. The product was dried at 60 °C in vacuum oven and named as BaTiO$_3$-CdS(20 wt%). BaTiO$_3$-CdS with different weight ratios (10 and 30 wt%) of CdS to BaTiO$_3$ were synthesized in a similar way except for the amounts of Cd and S. In addition, the pure CdS can be obtained through the similar chemical bath process without introducing BaTiO$_3$. For comparison, silica with the similar particle size of BaTiO$_3$ was synthesized by the previous reported method [49]. The corresponding SiO$_2$-CdS (20 wt%) composite was conducted under the same conditions as the BaTiO$_3$-CdS (20 wt%).

2.2. Characterization

Crystal structure identification was performed using Bruker D8 Advance X-ray diffractometer (XRD) with Cu Kα radiation (λ = 0.15418 nm) which operated at 40 kV and 40 mA. Morphologies of the samples were measured by a field-emission scanning electron microscope (SEM; FEI NovaNanoSEM-230). Microstructures were investigated using transmission electron microscopy (TEM) measured on a TecnaiG2F20 S-TWIN (FEI company) with a field emission gun at 200 kV. The optical properties of the samples were analyzed by UV–vis diffuse reflectance spectroscopy (UV-vis DRS) using a UV–vis spectrophotometer (Cary 5000, Agilent), in which BaSO$_4$ was used as the background.

Electrochemical analysis was conducted using a ZENNIUM electrochemical workstation (Zahner, Germany) with a conventional three-electrode system. The counter and reference electrodes were Pt plate and Ag/AgCl, respectively, and 0.2 M Na$_2$SO$_4$ (pH = 6.8) aqueous solution served as the electrolyte. 5 mg of the as-prepared sample and 20 μL nafion reagent was dispersed in 0.5 mL N,N-dimethyl formamide (DMF) solution by sonication, and the slurry was then evenly deposited in a 0.5 × 0.5 cm^2 window onto an indium tin oxide (ITO) conductor glass substrate to serve as a working electrode. A 300 W xenon lamp equipped with a 400 nm filter was used to provide a visible light source.

2.3. Photocatalytic H$_2$ evolution

Photocatalytic activity of each sample was done by photocatalytic H$_2$ evolution with a top-irradiation reaction vessel connected to a closed gas circulation system. Typically, 20 mg of the photocatalyst powder was dispersed in 100 mL aqueous solution containing 0.1 M Na$_2$S and 0.1 M Na$_2$SO$_3$ under magnetic stirring. The system was degassed for 1 h before irradiation. Then, the reaction was carried out under the irradiation of a 300 W Xe lamp with a 400 nm cutoff filter
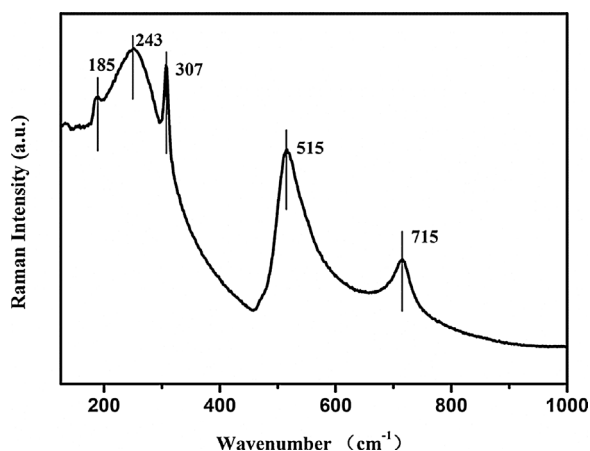
Fig. 1. Raman spectrum of $BaTiO_3$ nanospheres.

(power density = 0.55 W/cm^2). The hydrogen was detected by a Techcomp GC7900 gas chromatograph with a thermal conductivity detector (TCD).

3. Results and discussion

3.1. Characterization

BaTiO$_3$ nanospheres were synthesized using a sol-gel hydrothermal method [48]. The X-ray diffraction pattern of the as-synthesized sample shown in Fig. S1 can be well indexed as tetragonal BaTiO$_3$ with space group P4mm (JCPDS card 81-2201). The peak splitting of (002) and (200) at $2\theta \sim 45°$ confirms that the as-prepared sample is tetragonal ferroelectric BaTiO$_3$ (insert in Fig. S1). Furthermore, Raman spectrum, which has been utilized as a powerful tool to investigate the tetragonal-cubic phase transition, further confirms the existence of tetragonal ferroelectric BaTiO$_3$ [50]. As the Raman spectrum (Fig. 1) shown, the peaks at 515, 243, 185 cm^{-1} are assigned to the fundamental TO mode of A$_1$ symmetry. The peak at 307 cm^{-1} to B$_1$ mode indicates the asymmetry of BaTiO$_3$ within the TiO$_6$ octahedra on a local scale and the peak around 715 cm^{-1} is related to the highest frequency longitudinal optical mode (LO) with A$_1$ symmetry. These typical peaks indicate that the as prepared BaTiO$_3$ nanoparticles are tetragonal phase, which is closely agree with the reported literature of tetragonal BaTiO$_3$ nanopowder [50,51]. As illustrated in Fig. 2, peaks appearing in the original CdS particles can be indexed to wurtzite CdS (JCPDS card 89-0440). No detected peaks of impurities are observed. As for BaTiO$_3$-CdS, the diffraction peaks are similar to that of pure BaTiO$_3$, those are well-
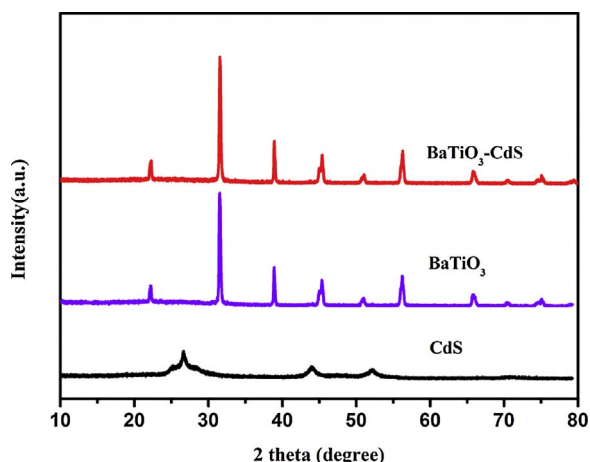

Fig. 2. Typical XRD patterns of CdS, BaTiO$_3$ and BaTiO$_3$-CdS (20 wt%) composite.

matched with tetragonal BaTiO$_3$. It demonstrated that BaTiO$_3$ maintains the essential crystal structure after the chemical bath deposition CdS particles. However, no obvious diffraction peaks belonging to CdS crystal are detected in the XRD of BaTiO$_3$-CdS composite. The possible cause is that the diffraction intensity of CdS is too weak to be detected, compared to that of BaTiO$_3$ crystal.

As shown in the SEM (Fig. S2) and TEM (Fig. 3) images, well-crystallized hemispheric CdS nanoparticles grow onto the surfaces of the BaTiO$_3$ nanospheres to form the hybrid nanoparticles. SEM image of pure BaTiO$_3$ shows essentially the same smooth surface morphology composing of closely spheres with a particle size of 80–110 nm. After deposited with CdS particles, the surfaces of BaTiO$_3$ becomes rough, which indicates a uniform deposition of CdS on the BaTiO$_3$ nanospheres. It is found from TEM images that the CdS nanoparticles in BaTiO$_3$-CdS samples are anchored over the BaTiO$_3$ hosts and have a narrow distribution in average size of ∼10 nm. High-resolution TEM (HRTEM) image shows the characteristic spacing of 0.316 and 0.336 nm respectively, corresponding to the (101) and the (002) lattice planes of wurtzite CdS [52]. Simultaneously, the lattice fringes of BaTiO$_3$-CdS display interplanar distance of 0.399 and 0.403 nm, matches well with that of the (100) and the (001) planes of the tetragonal BaTiO$_3$, respectively [29], further confirming that the BaTiO$_3$ crystal possesses a tetragonal P4mm structure. Besides, as the selected area electron diffraction (SAED) image displayed in Fig. 2d, the diffraction spots referred to (100) and (001) planes of BaTiO$_3$ were observed, indicating that BaTiO$_3$ nanospheres show single-crystal characteristics. The existence of Ba, Ti, O, Cd, and S elements was also certified by energy-dispersive X-ray spectrometry (EDX) (see Fig. S5).

3.2. Photocatalysis

In order to demonstrate the effect of the built-in electric field of ferroelectric BaTiO$_3$ on charge carrier separation of CdS, photocatalytic H$_2$ evolution was measured under visible light irradiation ($\lambda \geq 400$ nm) to evaluate the photocatalytic activity of the aforementioned products. Fig. 4a shows a comparison of visible light photocatalytic hydrogen production rates between pure BaTiO$_3$, CdS and BaTiO$_3$-CdS composite. It can be found that no H$_2$ can be detected when BaTiO$_3$ alone is used as catalyst. So, pure BaTiO$_3$ is inactive and could not reduce water to H$_2$ under the experimental conditions. The reason is that the band gap of BaTiO$_3$ is too wide to be stimulated in visible-light region. As a member of narrow bandgap semiconductors, pure CdS also shows a low photocatalytic activity, which could be assigned to the rapid recombination of photoexcited electrons and holes. Nevertheless, BaTiO$_3$-CdS composite exhibits a much higher activity of H$_2$ production than either BaTiO$_3$ or CdS individually. After introducing a small amount of CdS particles on BaTiO$_3$, the activity of the obtained composite sample is remarkably enhanced. It is worthwhile mentioning that there is an optimal loading amount of CdS in terms of photocatalytic performance. The supreme photocatalytic hydrogen production rate of BaTiO$_3$-CdS composites, 483 μmol h^{-1} g^{-1}, is observed when CdS is loaded to 20 wt%. This rate of BaTiO$_3$-CdS(20 wt%) is about 9.7 times that of CdS independently. This activity rules are possibly caused by the combined effects of the following factors: low loading of CdS (10 wt%) results in a decreased density of active sites for H$_2$ evolution. With the content of CdS increased to 20 wt%, the catalytic activity improvements with the increase of active sites. At this situation, numerous island-like morphology of CdS are anchored on the surface of BaTiO$_3$, which is exposed in the solution and fully contacted with H$_2$O and sacrificial agent (see Fig. 5a). However, excessive CdS may form a stacked structure when a further increasing CdS to 30 wt% (see Fig. 5b), which results in a reduced specific surface area of CdS to participate in a redox reaction. The limited contact between solution and electrons/holes on CdS may account for the deterioration of photocatalytic performance at higher CdS loading (see TEM images of BaTiO$_3$-CdS (30 wt%) composite in Fig. 6). Meanwhile, the influence of BaTiO$_3$ spontaneous polarization electric
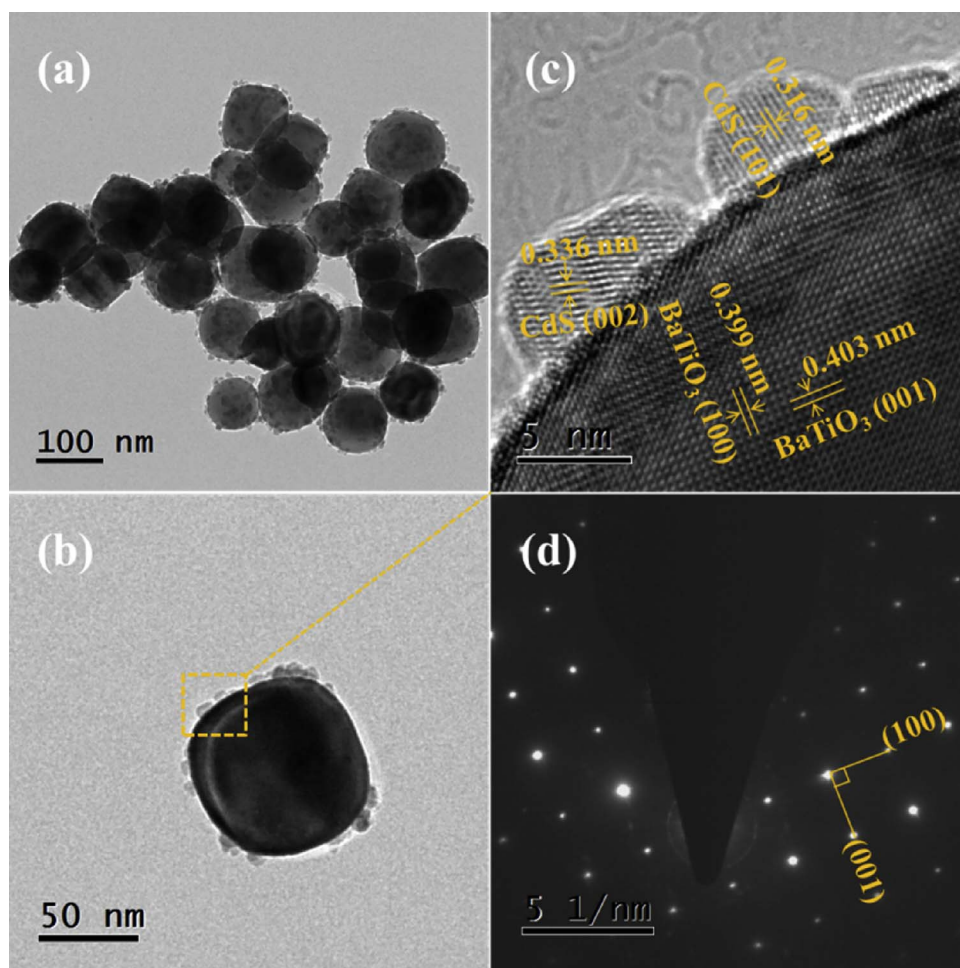
field on CdS would decrease with the increase of distance between BaTiO$_3$ and CdS. That is, the carriers separation driven by polarization electric field in CdS would be weakened as increasing the stacked thickness of CdS.

To further confirm that the function of tetragonal BaTiO$_3$ core, contrast experiments are conducted using SiO$_2$-CdS (20 wt%) composite structure catalyst processed under the same conditions as the BaTiO$_3$-CdS (20 wt%) powers (See Fig. S3). As shown in Fig. 4b, the hydrogen evolution efficiency of BaTiO$_3$-CdS (20 wt%) is almost 17.7 times as

high as that of SiO$_2$-CdS (20 wt%). Besides, photocatalytic activity of SiO$_2$-CdS (20 wt%) composite is even lower than pure CdS. These findings indicate that the BaTiO$_3$ core indeed play a significant role in the performance of the hybrid photocatalysts, likely owing to the dipolar fields from the ferroelectric domains of the core. In this system, specific surface area of SiO$_2$ may be responsible for the increased photocatalytic activity. Considering the specific surface area is one of the important factors that affect the activities of the photocatalysts. Usually, the larger specific surface area, the higher activity of the
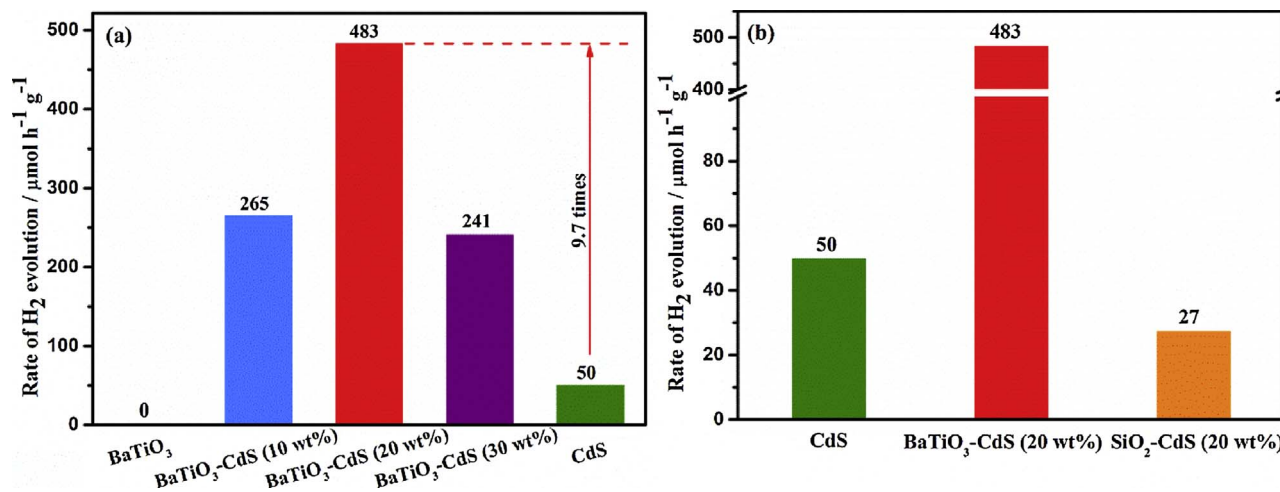

Fig. 4. Rate of H$_2$ evolution on (a) pristine BaTiO$_3$ nanospheres, BaTiO$_3$-CdS composites (10, 20 and 30 wt%), and pure CdS and on (b) pure CdS, SiO$_2$-CdS (20 wt%) and BaTiO$_3$-CdS (20 wt%) composites.
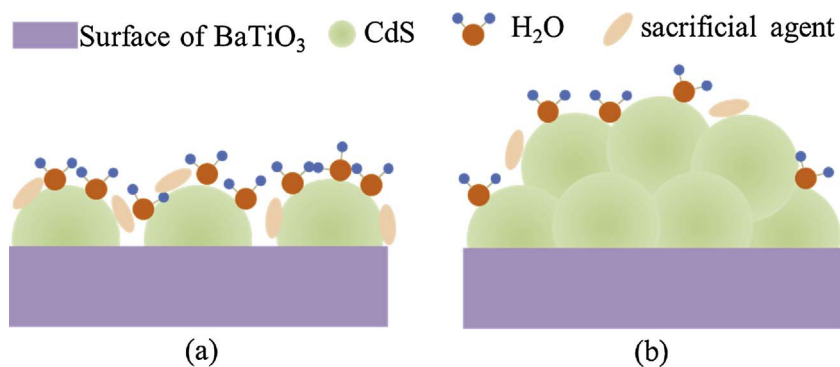
Fig. 5. Schematic showing the influence of the content of CdS; (a) a small amount of CdS is in full contact with H_2O and sacrificial agent in solution; (b) excessive CdS is stacking on the surface of $BaTiO_3$.
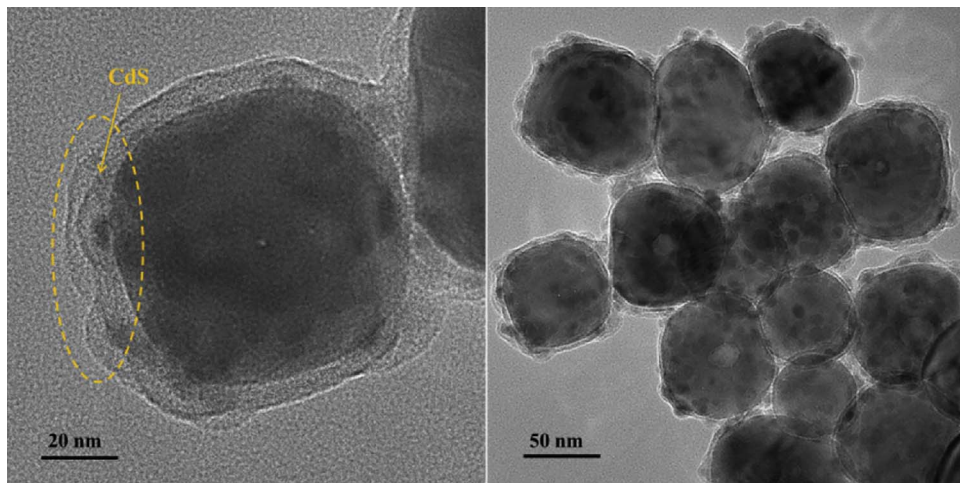

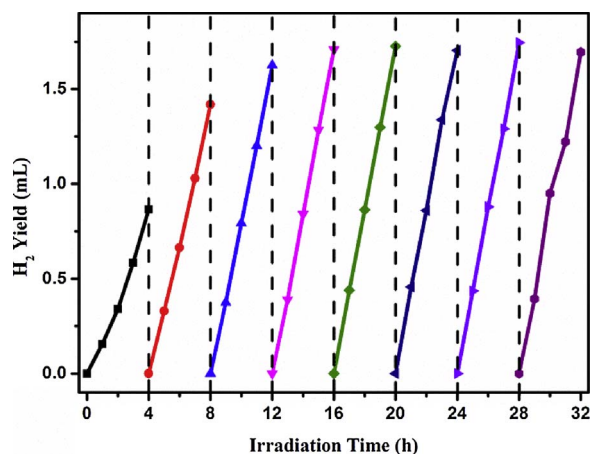**Fig. 6.** TEM images of $BaTiO_3$-CdS (30 wt%) composite.

Fig. 7. Time-circle photocatalytic H_2 evolution rate on $BaTiO_3$-CdS (wt 20%) composite.

Fig. 8. Schematic of photoinduced hole and electron migration in $BaTiO_3$-CdS composites and photocatalytic hydrogen process under visible light ($\lambda > 400$ nm).

photocatalysts. Then we evaluated the specific surface area of samples by BET measurements (See Fig. S4). The specific surface areas of $BaTiO_3$-CdS (20 wt%) (9 m^2/g) and $BaTiO_3$ (8 m^2/g) samples exhibit only small difference. However, SiO_2-CdS (20 wt%) (34 m^2/g) is three times more than the previous two samples, which does not fit the trend of H_2 evolution performances. These results indicate that the specific surface area is not the main factor for photocatalytic performance in $BaTiO_3$-CdS systems.

The stability is among the most important aspects for photocatalysts. Notably, as shown in Fig. 7, $BaTiO_3$-CdS (20 wt%) present a satisfying stable performance of hydrogen production during a 32 h cycling test without refreshing the catalysts and sacrificial agents. It is mentioning that the rate of H_2 evolution is much lower at the beginning
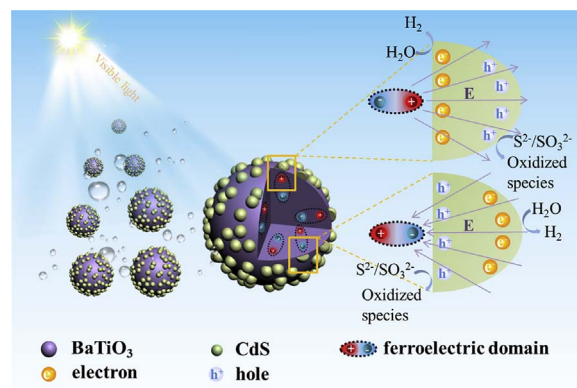
of irradiation than that in the subsequent progress. To determine the damage caused by photocorrosion, XRD and TEM patterns of $BaTiO_3$-CdS (20 wt%) after 32 h cycling test of photocatalytic hydrogen production were recorded, and the result is shown in Figs. S6, S7. It can be seen that the crystal structure remains intact, and no obvious change in surface morphology. This result implies that $BaTiO_3$ core efficiently restrain CdS from photocorrosion during the photocatalytic process, leading to an excellent photocatalytic stability.

3.3. Mechanism of photocatalytic activity enhancement

Based on the aforementioned experimental results, a tentative mechanism why $BaTiO_3$-CdS composites show significantly photocatalytic performance is formulated and displayed in Fig. 8. It is reported that ferroelectric polarization can influence the reactivity of a thin non-
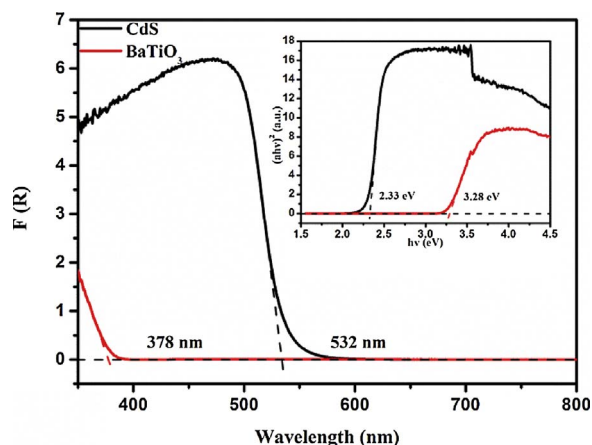
Fig. 9. UV–vis diffuse reflectance spectrum of BaTiO$_3$ and CdS. Inset is Tauc's plot of $(\alpha h\nu)^2$ versus photon energy for optical band-gap calculations.

Fig. 11. Conduction band and valence band potentials of BaTiO$_3$ and CdS.

ferroelectric coating [27,53]. The influence of the substrate was diminished as the film thickness increases and it eventually disappears when the film thickness exceeds 100 nm [54]. Here, the size of CdS particles on BaTiO$_3$ is less than 100 nm. Therefore, CdS will be influenced by the internal polar domains from ferroelectric in BaTiO$_3$-CdS hybrid photocatalyst. Photoexcited electrons and holes from excited CdS under visible light ($\lambda > 400$ nm) would be separated and transported effectively under the interaction of electric field driving force. These results vividly demonstrate that the ferroelectric polarization of BaTiO$_3$ plays an important role in enhancing the photocatalysis performance by increasing charge separation.

It is reported that the heterojunctions formed between two semiconductor photocatalysts with matched energy band structures can be favorable for the separation of the photoinduced charge carriers [55–58]. As we all known that CdS-sensitized semiconductor composite (e.g., CdS/TiO$_2$) can generate large amounts of H$_2$ because of the enhanced charge separation, which is due to the heterojunction structure [59–62]. Hence the energy structures of BaTiO$_3$ and CdS should be surveyed firstly. The optical absorbance of BaTiO$_3$ and CdS is measured using UV–vis absorption spectra (See Fig. 9). The optical absorbance of BaTiO$_3$ and CdS is measured using UV–vis absorption spectra (See Fig. 9). The absorption edge of BaTiO$_3$ is about 378 nm, while that of CdS is at about 532 nm. The following formula can be used to calculate the bandgap energy for one semiconductor [63].

$$\alpha h\nu = A(h\nu - E_g)^{n/2} \tag{1}$$

where $h\nu$, α, A, and E_g are light energy, absorption index, constant
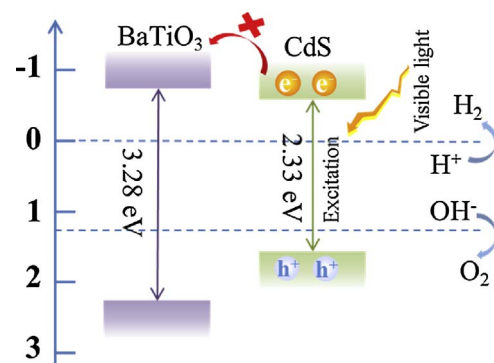
value, and band-gap energy of semiconductor, respectively. What is more, n relies on the transition type of semiconductor. The n for direct transition is equal to 1, while n is 4 for indirect transition. Therefore, the values of BaTiO$_3$ and CdS are all 1 [64,65]. According to inset of Fig. 9, BaTiO$_3$ is 3.28 eV, while E$_g$ of CdS is found to be about 2.33 eV.

As Fig. 10a shown, the valence band (VB) potential of BaTiO$_3$ and CdS, obtained by XPS method, are 1.94 and 1.13 V, respectively. That is, CdS possesses a more positive VB than BaTiO$_3$. The difference in the conduction band (CB) potentials for the two semiconductors can be revealed by measuring the flat-band potentials. As is shown in the Mott-Schottky curves (See Fig. 10b), the flat-band potentials are -1.04 and -0.86 V versus Ag/AgCl electrodes for BaTiO$_3$ and CdS, respectively. Then the CB of BaTiO$_3$ is more negative than that of CdS. Thus, a Type I traditional heterojunction can be formed between BaTiO$_3$ and CdS (energy band diagram can be expressed as Fig. 11). BaTiO$_3$ cannot be excited by visible light irradiation owing to its large band gap. Therefore, photocatalytic hydrogen production by BaTiO$_3$-CdS composite can be attributed only to electrons photo-generated from CdS. Once CdS is intrinsically activated by the photon energy to generate electron-hole pairs, electrons in the CB of CdS cannot drift into that of BaTiO$_3$. That is to say, due to the dis-matched energy levels, BaTiO$_3$ and CdS cannot form as conventional heterojunction, where charge transfer between two semiconductors ascribe to difference in VB and CB positions, to effectively separate photoinduced charge carriers of CdS. Hence, there must be another reason is responsible for the enhancement of performance.

Ferroelectric material has a self-polarization field (internal polar domains), which may play a critical role in charge separation process in composite materials. When ferroelectric material contacts with another semiconductor, the self-polarization could induce free carriers redistribution in the semiconductor. On the basis of experimental results and
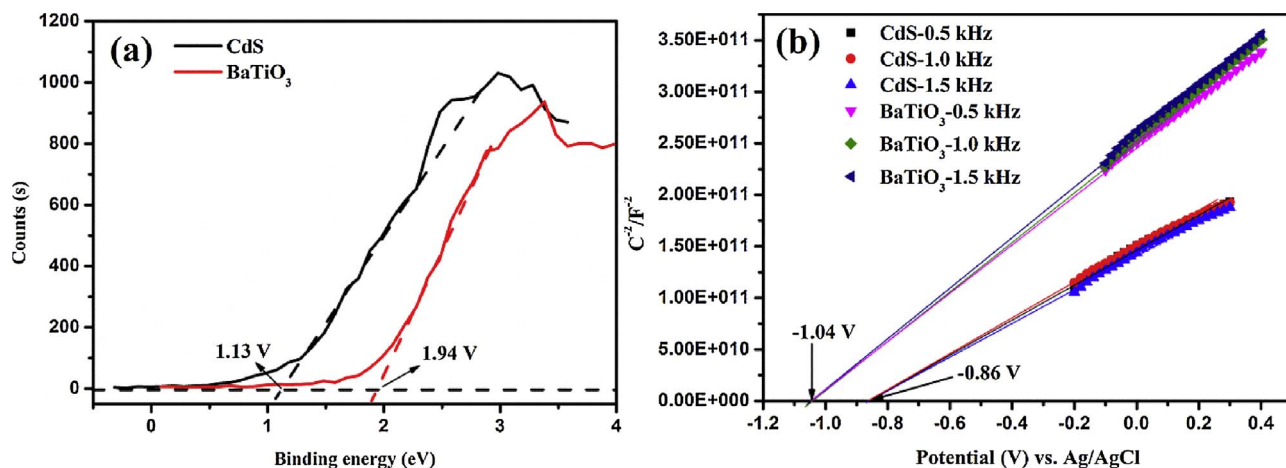

Fig. 10. (a) XPS valence band spectra of CdS and BaTiO$_3$. (b) Mott-Schottky curves of CdS and BaTiO$_3$ electrodes.
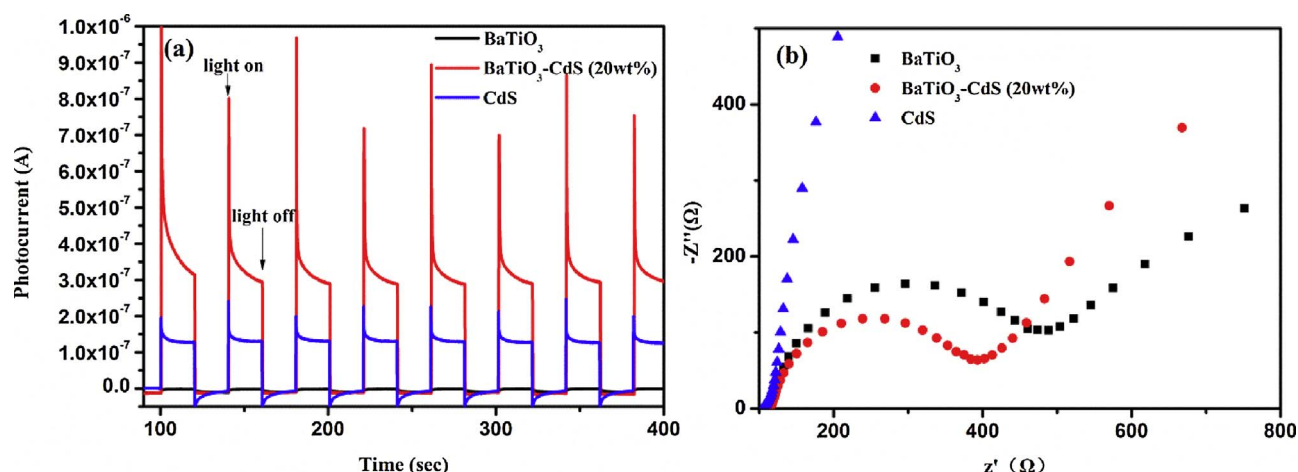
Fig. 12. Photoelectrochemical properties of pristine CdS, pure BaTiO₃ and BaTiO₃-CdS (wt 20%) composite. (a) Transient photocurrent responses of the samples in 0.2 M Na₂SO₄ versus Ag/AgCl electrodes at visible light illumination (λ > 400 nm). (b) EIS Nyquist plots of the samples.

mechanism analysis, we believe that the increased photocatalytic performance of BaTiO₃-CdS composites is accredited to valid separation and transmission of photoexcited electron-hole pairs by internal polar domains of ferroelectric materials. This hypothesis can be confirmed by photoelectrochemical tests. As shown in Fig. 12a, the clear photocurrent response is detected for two samples under visible-light irradiation. It is worth noting that pure CdS particles show a quite low photocurrent density, while the transient photocurrent response is significantly enhanced after assembling BaTiO₃ as a core. The photocurrent is primarily decided by efficient separation of photoexcited electrons and holes within the photoelectrode. Hence, the improved photocurrent means that more effective charge separation and transmission were realized after formation of BaTiO₃-CdS composites, which induced a prominent increment of photocatalytic performance in the photocatalytic hydrogen process. Electrochemical impedance spectroscopy (EIS) was also performed to further prove these results. As displayed in Fig. 12b, the impedance radius of BaTiO₃-CdS composites is smaller than that of CdS, which further confirms that the BaTiO₃ can efficiently reduce the charge recombination on the electrode/electrolyte interface. Besides, room temperature photoluminescence (PL) spectroscopy is also employed to get information on the influences of ferroelectric on the charge carrier dynamics. The detail discussion is presented in Supporting information.

All this results clearly indicate that the high rate of H₂ production in BaTiO₃-CdS composites can be ascribed to the presence of ferroelectric spontaneous polarization electric field of BaTiO₃.

4. Conclusion

In summary, BaTiO₃-CdS hybrid photocatalysts were successfully prepared via a hydrothermal and coprecipitation process. BaTiO₃-CdS composites displayed outstanding photocatalytic performance. The highest H₂ production rate was $483\,\mu mol\,h^{-1}\,g^{-1}$ when the loading amount of CdS was 20 wt%, which is about 9.7 times that of pure CdS. The improved activity is attributed to the improved separation ability of photoexcited carriers by the spontaneous polarization electric field of BaTiO₃. It is demonstrated that ferroelectric spontaneous polarization electric field can be applied as a build-in electric field to directly separate and transport the photogenerated electrons and holes. The achievements and findings in this work are expected to contribute to design more efficient photocatalyst systems through controlling internal fields.

Acknowledgements

Appendix A. Supplementary data

Supplementary data associated with this article can be found, in the online version, at https://doi.org/10.1016/j.apcatb.2018.01.036.

References

[1] N.S. Lewis, D.G. Nocera, Proc. Natl. Acad. Sci. 103 (2006) 15729–15735.
[2] H. Tong, S. Ouyang, Y. Bi, N. Umezawa, M. Oshikiri, Adv. Mater. 24 (2012) 229–251.
[3] T. Tachikawa, S. Yamashita, T. Majima, J. Am. Chem. Soc. 133 (2011) 7197–7204.
[4] A.L. Linsebigler, G. Lu, J.T. Yates Jr., Chem. Rev. 95 (1995) 735–758.
[5] W. Dong, Y. Yao, L. Li, Y. Sun, W. Hua, G. Zhuang, D. Zhao, S. Yan, W. Song, Appl. Catal. B: Environ. 217 (2017) 293–302.
[6] M. Farbod, M. Kajbafvala, Appl. Catal. B: Environ. 219 (2017) 344–352.
[7] Y. Wang, R. Shi, J. Lin, Y. Zhu, Energy Environ. Sci. 4 (2011) 2922.
[8] E.S. Elmolla, M. Chaudhuri, J. Hazard. Mater. 173 (2010) 445–449.
[9] H. Mou, C. Song, Y. Zhou, B. Zhang, D. Wang, Appl. Catal. B: Environ. 221 (2018) 565–573.
[10] A. Di Mauro, M. Cantarella, G. Nicotra, V. Privitera, G. Impellizzeri, Appl. Catal. B: Environ. 196 (2016) 68–76.
[11] Q. Xiang, G.F. Meng, H.B. Zhao, Y. Zhang, H. Li, W.J. Ma, J.Q. Xu, J. Phys. Chem. C 114 (2010) 2049–2055.
[12] P.M. Rao, L. Cai, C. Liu, I.S. Cho, C.H. Lee, J.M. Weisse, P. Yang, X. Zheng, Nano Lett. 14 (2014) 1099–1105.
[13] Y. Su, Z. Han, L. Zhang, W. Wang, M. Duan, X. Li, Y. Zheng, Y. Wang, X. Lei, Appl. Catal. B: Environ. 217 (2017) 108–114.
[14] W. Yu, J. Chen, T. Shang, L. Chen, L. Gu, T. Peng, Appl. Catal. B: Environ. 219 (2017) 693–704.
[15] T. Hisatomi, J. Kubota, K. Domen, Chem. Soc. Rev. 43 (2014) 7520–7535.
[16] S.J.A. Moniz, S.A. Shevlin, D.J. Martin, Z.-X. Guo, J. Tang, Energy Environ. Sci. 8 (2015) 731–759.
[17] H. Chen, D. Jiang, Z. Sun, R.M. Irfan, L. Zhang, P. Du, Catal. Sci. Technol. 7 (2017) 1515–1522.
[18] D.P. Kumar, S. Hong, D.A. Reddy, T.K. Kim, J. Mater. Chem. A 4 (2016) 18551–18558.
[19] S. Bai, L. Yang, C. Wang, Y. Lin, J. Lu, J. Jiang, Y. Xiong, Angew. Chem. Int. Ed. 54 (2015) 14810–14814.
[20] J. Liu, Q. Jia, J. Long, X. Wang, Z. Gao, Q. Gu, Appl. Catal. B: Environ. 222 (2018) 35–43.
[21] Y. Lv, X. Cao, H. Jiang, W. Song, C. Chen, J. Zhao, Appl. Catal. B: Environ. 194 (2016) 150–156.
[22] J. Schneider, M. Matsuoka, M. Takeuchi, J. Zhang, Y. Horiuchi, M. Anpo, D.W. Bahnemann, Chem. Rev. 114 (2014) 9919–9986.
[23] J. Li, L. Cai, J. Shang, Y. Yu, L. Zhang, Adv. Mater. 28 (2016) 4059–4064.
[24] D. Tiwari, S. Dunn, J. Mater. Sci. 44 (2009) 5063–5079.
[25] Y. Yuan, T.J. Reece, P. Sharma, S. Poddar, S. Ducharme, A. Gruverman, Y. Yang, J. Huang, Nat. Mater. 10 (2011) 296–302.
[26] J.L. Giocondi, G.S. Rohrer, Top. Catal. 49 (2008) 18–23.
[27] L. Li, P.A. Salvador, G.S. Rohrer, Nanoscale 6 (2014) 24–42.

[28] Y. Cui, J. Briscoe, S. Dunn, Chem. Mater. 25 (2013) 4215–4223.
[29] H. Li, Y. Sang, S. Chang, X. Huang, Y. Zhang, R. Yang, H. Jiang, H. Liu, Z.L. Wang, Nano Lett. 15 (2015) 2372–2379.
[30] K. Wang, Z. Fang, X. Huang, W. Feng, Y. Wang, B. Wang, P. Liu, Chem. Commun. 53 (2017) 9765–9768.
[31] J.L. Giocondi, G.S. Rohrer, Chem. Mater. 13 (2001) 241–242.
[32] A. Bhardwaj, N.V. Burbure, A. Gamalski, G.S. Rohrer, Chem. Mater. 22 (2010) 3527–3534.
[33] J.L. Giocondi, G.S. Rohrer, J. Phys. Chem. B 105 (2001) 8275–8277.
[34] A.M. Schultz, Y. Zhang, P.A. Salvador, G.S. Rohrer, ACS Appl. Mater. Interfaces 3 (2011) 1562–1567.
[35] S. Dunn, D. Tiwari, P.M. Jones, D.E. Gallardo, J. Mater. Chem. 17 (2007) 4460.
[36] S.V. Kalinin, D.A. Bonnell, T. Alvarez, X. Lei, Z. Hu, J.H. Ferris, Nano Lett. 2 (2002) 589–593.
[37] W. Cui, Z. Xia, S. Wu, F. Chen, Y. Li, B. Sun, ACS Appl. Mater. Interfaces 7 (2015) 25601–25607.
[38] R. Su, Y. Shen, L. Li, D. Zhang, G. Yang, C. Gao, Y. Yang, Small 11 (2015) 202–207.
[39] B. Yang, Y. Yuan, P. Sharma, S. Poddar, R. Korlacki, S. Ducharme, A. Gruverman, R. Saraf, J. Huang, Adv. Mater. 24 (2012) 1455–1460.
[40] W. Yang, Y. Yu, M.B. Starr, X. Yin, Z. Li, A. Kvit, S. Wang, P. Zhao, X. Wang, Nano Lett. 15 (2015) 7574–7580.
[41] Y. Cui, J. Briscoe, Y. Wang, N.V. Tarakina, S. Dunn, ACS Appl. Mater. Interfaces 9 (2017) 24518–24526.
[42] X. Lin, J. Xing, W. Wang, Z. Shan, F. Xu, F. Huang, J. Phys. Chem. C 111 (2007) 18288–18293.
[43] Y. Yang, Y. Zhang, Z. Fang, L. Zhang, Z. Zheng, Z. Wang, W. Feng, S. Weng, S. Zhang, P. Liu, ACS Appl. Mater. Interfaces 9 (2017) 6950–6958.
[44] N. Zhang, S. Liu, X. Fu, Y.-J. Xu, J. Mater. Chem. 22 (2012) 5042.
[45] Z. Ai, G. Zhao, Y. Zhong, Y. Shao, B. Huang, Y. Wu, X. Hao, Appl. Catal. B: Environ. 221 (2018) 179–186.
[46] C. Zhu, C. Liu, Y. Zhou, Y. Fu, S. Guo, H. Li, S. Zhao, H. Huang, Y. Liu, Z. Kang, Appl.

Catal. B: Environ. 216 (2017) 114–121.
[47] J.J. Zhao, Y.H. Li, P.F. Liu, Y.L. Wang, X.L. Du, X.L. Wang, H.D. Zeng, L.R. Zheng, H.G. Yang, Appl. Catal. B: Environ. 221 (2018) 152–157.
[48] K.I. Park, M. Lee, Y. Liu, S. Moon, G.T. Hwang, G. Zhu, J.E. Kim, S.O. Kim, D.K. Kim, Z.L. Wang, K.J. Lee, Adv. Mater. 24 (2012) 2999–3004.
[49] L. Hao, C. Zhu, C. Chen, P. Kang, Y. Hu, W. Fan, Z. Chen, Synth. Met. 139 (2003) 391–396.
[50] U.A. Joshi, S. Yoon, S. Baik, J.S. Lee, J. Phys. Chem. B 110 (2006) 12249–12256.
[51] R. Asiaie, W. Zhu, S.A. Akbar, P.K. Dutta, Chem. Mater. 8 (1996) 226–234.
[52] J. Pan, J. Li, Z. Yan, B. Zhou, H. Wu, X. Xiong, Nanoscale 5 (2013) 3022–3029.
[53] H. Huang, S. Tu, X. Du, Y. Zhang, J. Colloid Interface Sci. 509 (2017) 113–122.
[54] N.V. Burbure, P.A. Salvador, G.S. Rohrer, Chem. Mater. 22 (2010) 5823–5830.
[55] H. Liu, D. Chen, Z. Wang, H. Jing, R. Zhang, Appl. Catal. B: Environ. 203 (2017) 300–313.
[56] W. Feng, Y. Wang, X. Huang, K. Wang, F. Gao, Y. Zhao, B. Wang, L. Zhang, P. Liu, Appl. Catal. B: Environ. 220 (2018) 324–336.
[57] O.F. Lopes, K.T.G. Carvalho, A.E. Nogueira, W. Avansi, C. Ribeiro, Appl. Catal. B: Environ. 188 (2016) 87–97.
[58] S.A. Rawool, M.R. Pai, A.M. Banerjee, A. Arya, R.S. Ningthoujam, R. Tewari, R. Rao, B. Chalke, P. Ayyub, A.K. Tripathi, S.R. Bharadwaj, Appl. Catal. B: Environ. 221 (2018) 443–458.
[59] J.S. Jang, S.M. Ji, S.W. Bae, H.C. Son, J.S. Lee, J. Photochem. Photobiol. A: Chem. 188 (2007) 112–119.
[60] V.M. Daskalaki, M. Antoniadou, G. Li Puma, D.I. Kondarides, P. Lianos, Environ. Sci. Technol. 44 (2010) 7200–7205.
[61] J. Jang, H. Gyukim, P. Borse, J. Lee, Int. J. Hydrogen Energy 32 (2007) 4786–4791.
[62] H. Fujii, M. Ohtaki, K. Eguchi, H. Arai, J. Mol. Catal. A–Chem. 129 (1998) 61–68.
[63] M.A. Butler, J. Appl. Phys. 48 (1977) 1914–1920.
[64] H. Matsuda, N. Kobayashi, T. Kobayashi, K. Miyazawa, M. Kuwabara, J. Non-Cryst. Solids 271 (2000) 162–166.
[65] L.J. Zhang, S. Li, B.K. Liu, D.J. Wang, T.F. Xie, ACS Catal. 4 (2014) 3724–3729.